Inorganic Chemistry

pubs.acs.org/IC

Article

In Situ-Generated Hollow CoFe-LDH/Co-MOF Heterostructure Nanorod Arrays for Oxygen Evolution Reaction

Guoying Yang, Yijin Song, Songde Han, Zhen-Zhen Xue, De-Xuan Liu, Ani Wang,* and Guoming Wang

Cite This: *Inorg. Chem.* 2024, 63, 5634−5641

Read Online

ACCESS | Metrics & More | Article Recommendations | Supporting Information

ABSTRACT: Assembling a heterostructure is an effective strategy for enhancing the electrocatalytic activity of hybrid materials. Herein, CoFe-layered double hydroxide and Co-metal−organic framework (CoFe-LDH/Co-MOF) hollow heterostructure nanorod arrays are synthesized. First, $[Co(DIPL)(H_3BTC)(H_2O)_2]_n$ [named as Co-MOF, DIPL = 2,6-di(pyrid-4-yl)-4-phenylpyridine, H_3BTC = 1,3,5-benzenetricarboxylic acid] crystalline materials with a uniform hollow structure were prepared on the nickel foam. The CoFe-LDH/Co-MOF composite perfectly inherits the original hollow nanorod array morphology after the subsequent electrodeposition process. Optimized CoFe-LDH/Co-MOF hollow heterostructure nanorod arrays display excellent performance in oxygen evolution reaction (OER) with ultralow overpotentials of 215 mV to deliver current densities of 10 mA cm^{-2} and maintain the electrocatalytic activity for a duration as long as 220 h, ranking it one of the non-noble metal-based electrocatalysts for OER. Density functional theory calculations validate the reduction in free energy for the rate-determining step by the synergistic effect of Co-MOF and CoFe-LDH, with the increased charge density and noticeable electron transfer at the Co−O site, which highlights the capability of Co-MOF to finely adjust the electronic structure and facilitate the creation of active sites. This work establishes an experimental and theoretical basis for promoting efficient water splitting through the design of heterostructures in catalysts.

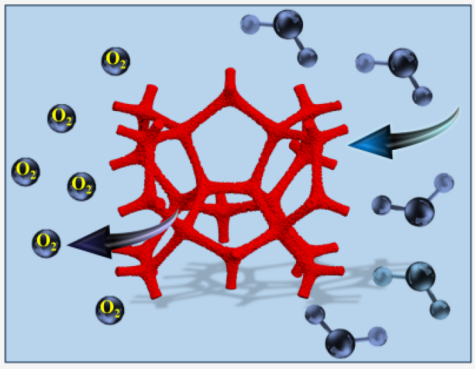

INTRODUCTION

The conversion of clean and renewable energy sources such as solar energy and wind energy into electrical energy, applied in the field of electrochemical water splitting, enables the large-scale production of high heating value and pollution-free hydrogen energy.[1,2] However, the slow kinetics of the oxygen evolution reaction (OER) at the anode hampers the energy efficiency of electrochemical water splitting, impeding its widespread application.[3,4] To date, considerable endeavors have been undertaken to fabricate low-cost, efficient, and enduring electrocatalysts that do not consist of precious metals for facilitating OER.[5−8] Especially, there is still a significant demand for the development of innovative approaches and designs for the synthesis of non-precious metal-based electrocatalysts that are highly efficient in promoting water splitting.

Heterojunctions with unique structures and properties have gained significant attention for their interfacial synergy. Compared to their individual components, heterojunctions exhibit distinct traits that make them valuable in materials science, catalysis, and energy research. The development of nanoscience and technology has led to various synthesis methods for heterojunctions, enabling more effective fundamental studies and practical applications.[9−11] Metal−organic frameworks (MOFs) possess inherent qualities such as facile accessibility of channels, active metal nodes that are evenly distributed, and a wide range of coordination environments,[12−15] which render them immensely versatile frameworks for fabricating transition metal-based electrocatalysts characterized by exceptional levels of efficiency.[16−19] Especially, Co-based MOFs have demonstrated great potential in OER.[20−22] Coincidentally, CoFe layer double hydroxide (LDH) has been widely recognized as an exceptionally efficient catalyst for OER, which can be attributed to the synergistic effects between Co and Fe metals, which significantly enhance the inherent reactivity of each active site.[23−26] The controlled and precise deposition of CoFe-LDH onto the surface of Co-based MOFs represents a promising strategy to enhance the catalytic activity for OER by synergistically harnessing the advantageous properties of both materials. However, the feasibility of fabricating CoFe-LDH/Co-MOF heterostructures with a hollow morphology and subsequently optimizing the local electronic structure to significantly augment the OER activity remains challenging.

Received: January 3, 2024
Revised: February 24, 2024
Accepted: February 26, 2024
Published: March 11, 2024

https://doi.org/10.1021/acs.inorgchem.4c00021
Inorg. Chem. 2024, 63, 5634−5641

Here, hollow CoFe-LDH/Co-MOF heterostructure nanorod arrays were constructed *in situ* on a nickel foam substrate. Interestingly, Co-MOF presents uniform hollow nanorod arrays with a transverse diameter of ∼100 nm grown on nickel foam; the CoFe-LDH/Co-MOF composite perfectly inherits the original hollow nanorod array morphology after the electrodeposition process. Benefiting from the hollow nanorod array structure, the synergistic effect of CoFe-LDH, Co-MOF, and CoFe-LDH/Co-MOF exhibits excellent OER intrinsic activity and stability in alkaline media. Density functional theory (DFT) calculations show that the CoFe-LDH/Co-MOF heterostructure can enhance the adsorption Gibbs free energy of oxygen-containing intermediates during OER, thereby facilitating electrocatalytic water splitting.

RESULTS AND DISCUSSION

The synthesis process of bimetallic CoFe-LDH/Co-MOF heterostructure nanorod arrays on the nickel foam substrate is shown in Figure 1a, which mainly includes the fabrication of CoO nanorod array templates, generation of hollow Co-MOF nanorod arrays (CoO as a self-sacrificial template to provide Co^{2+} ions and skeleton), and *in situ* conversion into CoFe-LDH/Co-MOF heterostructure nanorod arrays by a simple electrodeposition method (Figure S1, Supporting Information). The microstructures of the CoFe-LDH/Co-MOF heterostructure nanorod arrays were manifested by scanning electron microscopy (SEM) and transmission electron microscopy (TEM). First, Co-MOF presents uniform hollow nanorod arrays with a transverse diameter of ∼100 nm grown on nickel foam (Figure 1b,c), the obvious difference between the black shell and the lightful interior demonstrates the formation of uniform hollow architecture (Figure 1d), and the shell thickness of hollow nanorod Co-MOF is verified as ∼20 nm. The cavity size is about 70 nm, and none of the residual species remains in the cavity. Interestingly, the formation of the hollow interior can be also found as confirmed by a few broken nanorods with the just exposure of openings (Figure 1e and Figure S2). After the electrodeposition process is carried out, the CoFe-LDH/Co-MOF composite displays well-preserved hollow nanorod array morphology (termed as CoFe-LDH/Co-MOF heterostructure nanorod arrays), but the surface of the nanorod undergoes roughening and divides into numerous small particles (Figure 1f,g). The ordered and uniform structure of CoFe-LDH/Co-MOF can enhance the exposure of additional active regions and contact sites. The lattice spacing of 0.261 nm, observed in the high-resolution TEM (HRTEM) image (Figure 1h), agrees with the (012) crystal facet of CoFe-LDH. Additionally, the SAED patterns captured in the inset image of Figure 1h were examined and interpreted, indicating the presence of the (110) and (101) planes of CoFe-LDH. Simultaneously, (111) lattice fringes are observed at the outer edge, with an interplanar spacing of 0.403 nm, attributed to the interlayer distance of Co-MOF (the crystallographic data indicate a 0.403 nm interlayer distance). To acquire more comprehensive morphology information, the high-resolution TEM images clearly show the existence of many black nanoholes (marked by the green arrows), which confirm that the synthesized CoFe-LDH/Co-MOF nanostructure contains abundant defective sites (Figure 1i).[27] Meanwhile, energy-dispersive X-ray (EDX) spectroscopy elemental mapping analysis (Figure 1j) provides evidence that the Co, Fe, O, C, and N elements are evenly distributed throughout the CoFe-LDH/Co-MOF hollow nanorod arrays.

To investigate the growth mechanism of the hollow Co-MOF and CoFe-LDH/Co-MOF heterostructure nanorod arrays, TEM measurements were further conducted (Figure 2). Surprisingly, the core of CoO and the shell of the MOF are well observed at the beginning of the reaction, but as time prolonged, the CoO core interior collapsed obviously, yielding

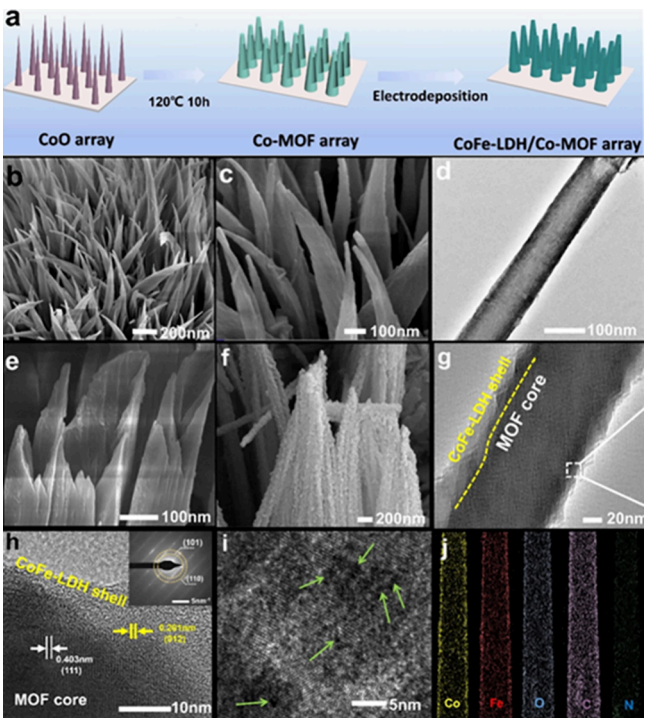

Figure 1. (a) Schematics of the formation of bimetallic CoFe-LDH/Co-MOF hollow heterostructure nanorod arrays on the NF substrate. (b, c) SEM and enlarged SEM images of the hollow Co-MOF template. (d) TEM images for the hollow Co-MOF template. (e) A few broken nanorods with the just exposure of openings for the Co-MOF template. (f) SEM image of the CoFe-LDH/Co-MOF heteronanotube array. (g) TEM image of the CoFe-LDH/Co-MOF heteronanotube array. (h) High-resolution TEM images of the CoFe-LDH/Co-MOF heteronanotube array. (i) High-resolution TEM image of the CoFe-LDH/Co-MOF nanostructure with abundant defective sites. (j) The distribution of elements within the CoFe-LDH/Co-MOF heteronanotube array was examined using energy-dispersive spectroscopy (EDS) and elemental mappings.

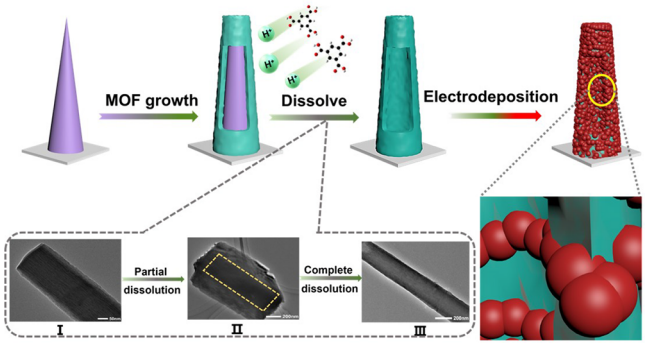

Figure 2. Model representation of the proposed mechanism of CoFe-LDH/Co-MOF formation (top). TEM images at different stages of Co-MOF formation (bottom) and graphical representation of the CoFe-LDH/Co-MOF heterostructure.

https://doi.org/10.1021/acs.inorgchem.4c00021
Inorg. Chem. 2024, 63, 5634−5641

an interior mesoporous arrangement (5 min); with the reaction time increased to 1 h, the internal collapse became more obvious, and finally, a clear hollow structure formed at 2 h. It is worth mentioning that in the solvothermal reaction process, 1,3,5-benzenetricarboxylic acid must be in excess to generate hollow morphology, as excess 1,3,5-benzenetricarboxylic acid can regulate the acidity of the solution and control the effective release of Co^{2+} ions in the CoO nanorod array and the collapse of the interior CoO nanorod (CoO is acid-labile in an acidic medium), which leads to an increasing number of Co^{2+} ions gathering on the surface of the CoO nanorod for coordination reactions.[28] The optimized amount of 1,3,5-benzenetricarboxylic acid to format the hollow structure is ca. 0.07 mmol, and the optimal pH range is 6.1−6.4. Based on the aforementioned findings and the disparity in stability between Co-MOF and CoO, our hypothesis revolves around an in-diffusion etching mechanism. Specifically, the formation of the hollow structure was attributed to the in-diffusion etching process induced by the dissociation of 1,3,5-benzenetricarboxylic acid, resulting in the release of H^+.[29,30] The CoO nanorod cores, sensitive to acid, undergo etching as H^+ ions accumulate and diffuse inwardly within the confined space, driven by the concentration gradient. In fact, the insufficient concentration of H^+ will not induce any etching of the Co-MOF (Figure S3). For the hollow CoFe-LDH/Co-MOF with a rough surface, during the electrodeposition process, the formation of a CoFe-LDH/Co-MOF heterogeneous nanotube array occurs on the surface of the Co-MOF nanorod array, which will not change the hollow structure of the Co-MOF nanorods, and thus, the hollow structure is naturally preserved. Notably, the hollow structure can provide more active sites and contact areas, thereby improving the catalytic performance.[31−34]

Single crystal X-ray diffraction reveals that Co-MOF $[Co(DIPL)(H_3BTC)(H_2O)_2]_n$ crystallize in the monoclinic $C2/c$ space group. Notably, Co-MOF is a novel single crystal, which has been synthesized for the first time with CCDC reference number 2301027.[35−38] The asymmetric units contain one deprotonated $HBTC^{2-}$ ligand (H_3BTC = 1,3,5-benzenetricarboxylic acid), one DIPL ligand (DIPL = 2,6-di(pyrid-4-yl)-4-phenylpyridine), and one free water molecule. Co-MOF forms a two-dimensional layer (Figure S4) and a three-dimensional network supramolecular structure by interconnecting with Co^{2+} ions, H_3BTC, and DIPL ligands (Figure 3a,b). The detailed bond length and angle parameters of Co-MOF are shown in the Supporting Information (Tables S1 and S2). The structure of CoFe-LDH is presented in a ball-and-stick model in Figure 3c. X-ray diffraction (XRD) analysis was utilized to determine the phase characteristics of the CoFe-LDH/Co-MOF composite. The XRD patterns demonstrated a high degree of correlation between the signals observed for Co-MOF and CoFe-LDH (JCPDS no. 14-0235), with the exception of a prominent diffraction peak attributed to the nickel foam substrate; X-ray photoelectron spectroscopy (XPS) was employed to investigate the chemical valence states of the elements present in the CoFe-LDH/Co-MOF material (Figure S5), and the results confirmed the successful synthesis of the Co-MOF and CoFe-LDH composites, as further evidenced by the data presented in Figure 3d. As exhibited in Figure 3e, the deconvolution results of Fe 2p can be resolved into three distinct peaks, one obvious peak located at 706.5 eV can be assigned to Fe^{3+}, the peaks at 718.9 and 713.3 eV are attributed to Fe^{2+},[39−41] and no evidence of Fe−O bond formation between iron atoms and 1,3,5-benzenetricarboxylic acid was detected, suggesting a low concentration of iron species in the Co-MOF structure, which is in agreement with the results obtained from the XRD analysis. The binding energy at 532.4 eV corresponds to the surface-adsorbed H_2O, while the peak at 529.4 eV is indicative of the M−O bond characteristic.[27] Two evident peaks at 780.6 eV (Co $2p_{3/2}$) and 796.5 eV (Co $2p_{1/2}$) and two small peaks at 779.4 and 795.6 eV [Co(0)] of the Co 2p XPS spectrum are the typical characteristics of Co^{2+} and Co(0) species, respectively (Figure 3g).[42,43] Four fitting peaks of the deconvoluted XPS spectrum for C 1s located at 282.7, 285.6, 288.2, and 286.4 eV correspond to C−C/C═C, C═N, carboxyl, and carbonyl, respectively (Figure 3h),[44−47] and two peaks of the high-resolution N 1s spectrum appeared at 395.6 and 397.6 eV corresponding to pyridinic N and Co−N (Figure 3i).[48,49]

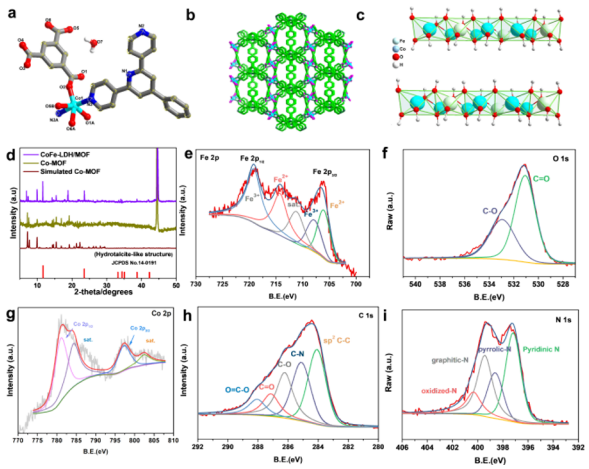

Figure 3. (a) Coordination environments for Co(II) ions in Co-MOF. (b) View of the 3D structure for Co-MOF. (c) Crystal structure of CoFe-LDH. (d) XRD patterns of Co-MOF, CoFe-LDH, and CoFe-LDH/Co-MOF. (e−i) XPS spectra of Fe 2p, O 1s, Co 2p, C 1s, and N 1s of CoFe-LDH/Co-MOF.

The OER electrocatalytic activities of the CoFe-LDH/Co-MOF heterostructure nanorod arrays, Co-MOF, CoFe-LDH, Ni@CoO, and the benchmark RuO_2/NF, nickel foam were evaluated in 1 M KOH electrolyte using a standard three-electrode system. From the polarization curves shown in Figure 4a, it can be observed that CoFe-LDH/Co-MOF exhibits the lowest overpotential of 215 mV at a current density of 10 mA·cm^{-2}. Conversely, to achieve the same level of current density, it is necessary to apply 246, 285, 310, and 372 mV for CoFe-LDH, Co-MOF, Ni@CoO, and the benchmark RuO_2, respectively. Furthermore, the CoFe-LDH/Co-MOF electrode exhibits a significantly lower Tafel slope of 43 mV·dec^{-1} compared to CoFe-LDH (65 mV·dec^{-1}), Co-MOF (83 mV·dec^{-1}), RuO_2 (112 mV·dec^{-1}), and Ni@CoO (148 mV·dec^{-1}) (Figure 4c). Various scanning rates were utilized to measure the double-layer capacitance (Cdl) via cyclic voltammetry (CV)[50−52] (Figure 4d and Figure S6). The Cdl value of CoFe-LDH/Co-MOF is 9.45 mF·cm^{-2}, much greater than those of CoFe-LDH (7.65 mF·cm^{-2}) and Co-MOF (4.57 mF·cm^{-2}) (Figure 4e). In addition, electrochemical methods were employed to measure and calculate the quantity of active sites in CoFe-LDH/Co-MOF and compare the turnover frequency (TOF) values of each distinct active site.[53,54] In general, a larger ECSA value suggests a greater number of exposed active sites. Consequently, the normalization of Cdl differential polarization curves can be useful in

https://doi.org/10.1021/acs.inorgchem.4c00021
Inorg. Chem. 2024, 63, 5634−5641

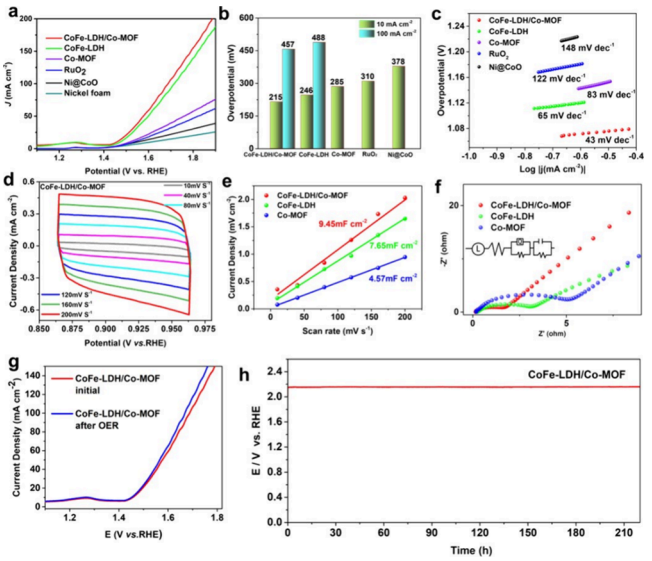

Figure 4. (a) OER polarization curves. (b) Overpotential diagram. (c) Tafel slope plots and (d) CV curves of the CoFe-LDH/Co-MOF heteronanotube array at different scan rates. (e) Electrochemical impedance spectra. (f) Electrochemical impedance spectroscopy. (g) LSV curves obtained for CoFe-LDH/Co-MOF. (h) Time overpotential curve under 10 mA·cm^{-2} for 220 h.

assessing intrinsic activity.[55,56] The ECSA-normalized LSV curves illustrate that CoFe-LDH/Co-MOF exhibits lower overpotentials compared with Co-MOF and CoFe-LDH (Figure S7), further confirming the superior intrinsic activity of CoFe-LDH/Co-MOF in the OER process. For comparison, CoFe-LDH/Co-MOF was prepared by varying the molar ratio of bimetal sources (named as Co*x*Fe-LDH/Co-MOF, where *x* is the molar ratio of $Co(NO_3)_2{\cdot}6H_2O/Fe(NO_3)_3{\cdot}9H_2O$). Note that among all the bimetallic Co*x*Fe-LDH/Co-MOF catalysts, Co*x*Fe-LDH/Co-MOF exhibits the highest OER catalytic activity (Figure S8).

It should be noted that the highest number of active sites was observed in CoFe-LDH/Co-MOF (4.053×10^{-7} mol), and its TOF value (0.195 s^{-1}) surpasses those of Co-MOF (0.132 s^{-1}) and CoFe-LDH (0.143 s^{-1}) at a 300 mV overpotential, which indicates that CoFe-LDH/Co-MOF exhibits the highest OER intrinsic activity. In addition, the representative Nyquist plots attribute the smallest charge resistance to the CoFe-LDH/Co-MOF heterostructure, which is considered to be the most suitable structure for efficient mass transfer and charge transfer kinetics with a minimum interfacial barrier, as depicted in Figure 4f. Long-term stability for the CoFe-LDH/Co-MOF heteronanotube array on the NF substrate was evaluated. After the 24 h durability test, the LSV curve indicated that the material retained about 98% of its activity (Figure 4g), and the catalytic stability was even maintained for 220 h with no appreciable deactivation (Figure 4h). The XRD spectra for the initial CoFe-LDH/Co-MOF after OER demonstrate similar peaks, indicating that the main framework of CoFe-LDH/Co-MOF is retained after electrochemical treatment (Figure S9). In comparison to similar catalysts, CoFe-LDH/Co-MOF exhibits outstanding superiority in terms of OER activity (as shown in Table S3), which signifies that the heterostructured CoFe-LDH/Co-MOF can function as a highly efficient catalyst for the oxygen evolution reaction in alkaline electrolytes. The distinctive heteronanotube array, enriched with plentiful defects, provides accessible active sites on the surface, thus facilitating mass transport and subsequent charge transfer during the OER process.

To gain insights into the underlying mechanism of catalytic reactions in CoFe-LDH/Co-MOF, thorough characterization was conducted on the morphological structure and chemical composition of CoFe-LDH/Co-MOF using a combination of XRD, Raman, XPS, SEM, and TEM techniques subsequent to the durability assessment. Continued research has been conducted on the mechanism of the water oxidation reaction in Co-based materials, with particular attention given to the single-site mechanism.[38,57,58] When exposed to alkaline conditions, the Co and Fe active sites first attract and bind OH− ions, leading to the formation of intermediates, such as Co−OH and Fe−OH. This process is also accompanied by the release of electrons. As a result, the Co−OH and Fe−OH intermediates undergo oxidation, ultimately giving rise to the creation of Co−O and Fe−O species. Subsequently, the Co−O and Fe−O bonds are subjected to attack by additional OH− ions, giving rise to the generation of CoOOH and FeOOH intermediates. Subsequently, the −OOH groups undergo further oxidation, resulting in the release of O_2, which indicates the successful culmination of the electrocatalytic oxidation reaction. According to the XPS spectral analysis, there was an observation of newly emerged Co^{3+} oxidation peaks and a slight shift toward higher binding energy in the Co 2p and Fe 2p spectra.[59] Additionally, the prominent peak observed in the O 1s spectra located at 530.3 eV can be attributed to the characteristic M−O bond present in oxyhydroxide compounds, indicating the formation and accumulation of CoOOH and FeOOH species (Figure 5a−c). Furthermore, Raman spectroscopy analysis (Figure 5d) revealed the presence of two distinct peaks that closely correspond to CoOOH (570.1 cm^{-1}) and FeOOH (476.3 cm^{-1}). Notably, after OER testing for 24 h, new lattice fringes were observed in the HRTEM image with the identified *d*-spacing values of 0.231 and 0.332 nm attributed to the (111) crystal plane of CoOOH and (310) lattice plane of FeOOH, respectively, which provide further support and validation results of the Raman and XPS tests (Figure 5e). These discoveries illustrate that Co^{2+} and Fe^{3+} of CoFe-LDH/Co-MOF act as the catalytic active sites and enhance the formation of CoOOH and FeOOH intermediates for OER during the electrocatalytic oxidation process. Figure 5f shows that the original morphology can be maintained, even after the electrocatalytic reaction is completed.

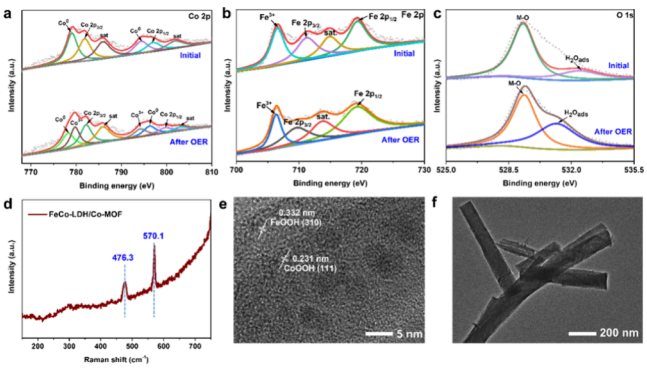

Figure 5. (a−c) High-resolution XPS spectra of CoFe-LDH/Co-MOF. (d) Raman spectrum, (e) high-resolution TEM image, and (f) SEM image of CoFe-LDH/Co-MOF after the OER test.

https://doi.org/10.1021/acs.inorgchem.4c00021
Inorg. Chem. 2024, 63, 5634−5641

To obtain a more comprehensive comprehension of the electrocatalytic behavior of CoFe-LDH/Co-MOF in the oxygen evolution reaction (OER), we performed density functional theory (DFT) calculations using Vienna Ab initio Simulation Package (VASP) software.[27] Previous research published in the scientific literature has suggested that the catalytic activity of CoFe-LDH in the oxygen evolution reaction (OER) is heavily influenced by the cobalt−oxygen (Co−O) sites, and the presence of additional species has been demonstrated to enhance its electrocatalytic performance.[60,61] It is important to highlight that during our DFT simulations, we opted to simplify the intricate periodic crystal structure of the CoFe-LDH/Co-MOF hybrid by focusing on a single Co-MOF monomer. The simplification was necessary due to the challenges associated with identifying active sites within the complex framework of the CoFe-LDH/Co-MOF hybrid, which is a time-consuming and intricate process. Moreover, the computational resources needed for such simulations are constrained. Therefore, it is reasonable to streamline the model by approximating the periodic crystal structure of Co-MOF as a monomer of the Co-MOF sheet. Recent research has presented compelling evidence to support the efficacy of this simplified methodology. Consequently, a CoFe-LDH/Co-MOF arrangement was established to examine the impact of the CoFe-LDH and Co-MOF interaction on the OER efficiency of the CoFe-LDH/Co-MOF hybrid. Our emphasis centered on the oxygen atom positioned in close proximity to the cobalt atom (referred to as the Co−O site), as depicted in Figure 6a,b. Comparatively, structural optimizations were also implemented for CoFe-LDH and Co-MOF (Figures S10 and S11, Supporting Information).

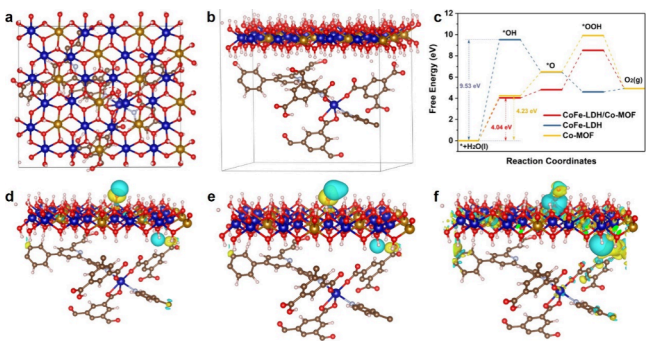

Figure 6. Schematic representation of the predicted adjacent reaction sites on CoFe-LDH/Co-MOF: (a) top view and (b) side view. (c) Relative energy diagram illustrating the oxygen evolution reaction (OER) on the cobalt−oxygen (Co−O) site on CoFe-LDH/Co-MOF, CoFe-LDH, and Co-MOF. Differential charge density analysis of (d) CoFe-LDH-O/Co-MOF, (e) CoFe-LDH−OH/Co-MOF, and (f) CoFe-LDH-OOH/Co-MOF sites (yellow and cyan represent charge accumulation and depletion, in which the Co, Fe, C, H, and N atoms are in purple, green, gray, light white, and light blue, respectively).

To explore how the catalytic performance of CoFe-LDH is affected by Co-MOF support, the CoFe-LDH/Co-MOF configuration was set up. Figure 6c shows the reaction pathway for the oxygen evolution reaction (OER) on the Co−O site of CoFe-LDH/Co-MOF, and it offers a comparison with CoFe-LDH and Co-MOF pathways. In the OER process, the rate-determining step (RDS) is often determined by identifying the step within the four-step reaction sequence that exhibits the largest alteration in Gibbs free energy (ΔG).[62−64] As illustrated in Figure 6c, the rate-determining steps (RDSs) for CoFe-LDH/Co-MOF, CoFe-LDH, and Co-MOF all involve the transformation of H_2O into OH*. The RDS for CoFe-LDH features a significant barrier in the initial reaction with a Gibbs free energy change of 9.53 eV. On the other hand, OH* adsorption at Co sites in Co-MOF is less strong than in CoFe-LDH, resulting in a decreased energy barrier (4.23 eV) for the conversion from H_2O to OH*, in contrast to CoFe-LDH.

On the other hand, the rate-determining step (RDS) at the Co adsorption site in the CoFe-LDH/Co-MOF heterostructure experiences similar modifications. The alterations in Gibbs free energy account for 4.04 eV, suggesting that the heterostructure with two-phase coupling can diminish the energy barrier, enhance the RDS, and consequently enhance the OER kinetics, which compellingly supports the existence of a synergistic effect between Co-MOF and CoFe-LDH. The analysis of differential charge density for CoFe-LDH-O/Co-MOF, CoFe-LDH−OH/Co-MOF, and CoFe-LDH-OOH/Co-MOF (as shown in Figure 6d−f) was performed, where regions in yellow indicate charge accumulation and regions in blue indicate charge depletion. The adsorption configurations of CoFe-LDH-O/Co-MOF, CoFe-LDH−OH/Co-MOF, and CoFe-LDH-OOH/Co-MOF can be found in Figure S12 of the Supporting Information. The Co−O site exhibits increased charge density and noticeable electron transfer, highlighting Co-MOF's ability to finely adjust the electronic structure and facilitate the creation of active sites. The DFT findings mentioned earlier offer proof that CoFe-LDH/Co-MOF surpasses individual Co-MOF and CoFe-LDH in terms of decreasing the adsorption Gibbs free energy of oxygen-containing intermediates during OER, which led to a greater enhancement of the OER activity.

CONCLUSIONS

In summary, novel CoFe-LDH/Co-MOF heterostructure nanorod arrays with abundant defects were designed for OER in alkaline media. CoFe-LDH/Co-MOF heterostructure nanorod arrays inherit and integrate the advantages of both CoFe-LDH and Co-MOF components such as abundant surface metallic sites, a uniform hollow structure, and high electrical conductivity for electrocatalysis. As a precatalyst enriched with abundant defective structures, CoFe-LDH/Co-MOF undergoes partial reconfiguration and generates CoOOH and FeOOH active species during the OER process. The unique behavior allows CoFe-LDH/Co-MOF to demonstrate excellent intrinsic electrocatalytic activity for OER in alkaline environments. The Co−O site exhibits increased charge density and noticeable electron transfer of CoFe-LDH/Co-MOF, highlighting the ability of Co-MOF to finely adjust the electronic structure. Our study presents a strategic approach for enhancing the efficiency of water electrolysis by capitalizing on the advantageous attributes of CoFe-LDH and Co-MOF materials, which establishes the foundation for direct water electrolysis utilizing nonprecious metal-based materials.

EXPERIMENTAL SECTION

Materials and General Methods. Cobalt nitrate hexahydrate ($Co(NO_3)_2{\cdot}6H_2O$) (99.99%) was purchased from MACKLIN. NH_4F (96.0%), urea (99.0%), and 1,3,5-trimesic acid (H_3BTC, 99%) were purchased from J&K Scientific. 2,6-Di(pyrid-4-yl)-4-phenylpyridine (98%), polyvinylpyrrolidone (PVP, M_w = 1,300,000), and potassium hydroxide (KOH) were purchased from Aladdin Ltd. (China). Ni

https://doi.org/10.1021/acs.inorgchem.4c00021
Inorg. Chem. 2024, 63, 5634−5641

foam was purchased from CeTech Co., Ltd. A. All the chemicals and materials were obtained from commercial sources and could be used without further purification.

Synthesis of Ni@CoO. The Ni@CoO nanorod arrays were synthesized as described previously without modifications.[65] A homogeneous solution was prepared by dissolving cobalt nitrate hexahydrate (582 mg), urea (600 mg), and ammonium fluoride (296 mg) in 36 mL of deionized water. The resulting homogeneous solution was then transferred into a stainless-steel autoclave with a Teflon lining, with a nickel foam (4 cm × 3.5 cm) inserted into the reaction solution. Subsequently, the autoclave was sealed and maintained at 120 °C for 10 h, followed by gradual cooling to room temperature. The resulting array sample was collected and subsequently rinsed multiple times with distilled water.

Synthesis of Co-MOF Arrays. The Ni@CoO nanorod array (1 cm × 1.5 cm) was introduced into a solution comprising 5 mL of deionized water containing homophenic acid (15 mg), 2,6-di(pyrid-4-yl)-4-phenylpyridine (15 mg), and polyethylpyrrolidone (10 mg). This mixture underwent a hydrothermal reaction at 120 °C for a duration of 10 h. Subsequently, the resulting array samples were collected, subjected to multiple rinses with distilled water, and subsequently dried in an oven maintained at 85 °C, which yielded the final product, named as Ni@CoO@Co-MOF.

Synthesis of CoFe-LDH/Co-MOF Arrays. CoFe-LDH nanoparticles were deposited onto Co-MOF array electrodes by using an electrodeposition technique. Prior to the electrodeposition experiments, a deposition solution was prepared by dissolving $Co(NO_3)_2 \cdot 6H_2O$ (20.95 mg) and $Fe(NO_3)_3 \cdot 9H_2O$ (11.61 mg) in 20 mL of deionized water. The electrodeposition process was carried out in this solution at a potential of 1.0 V versus Ag/AgCl for a duration of 300 s. The CoFe-LDH/Co-MOF electrode was then rinsed with deionized water and ethanol, followed by drying under vacuum conditions. CoFe-LDH/Co-MOF with different Co/Fe ratios was prepared as follows. A series of mixtures of $Co(NO_3)_2 \cdot 6H_2O$ and $Fe(NO_3)_3 \cdot 9H_2O$ (molar ratios of $Co(NO_3)_2 \cdot 6H_2O/Fe(NO_3)_3 \cdot 9H_2O$ are 1:0.5, 1:1, and 1:1.5) were prepared, and the electrodeposition process was carried out in the same process.

■ ASSOCIATED CONTENT

Supporting Information

The Supporting Information is available free of charge at https://pubs.acs.org/doi/10.1021/acs.inorgchem.4c00021.

> Pretreatment of Ni foam, synthesis of Co-MOF arrays, synthesis of CoFe-LDH/Co-MOF heterostructure nanorod arrays, images of Co-MOF arrays and CoFe-LDH/Co-MOF on the NF substrate, TEM images of the hollow interior confirmed by the broken nanorods with the just exposure of openings, TEM images of Co-MOF and CoO composite, two-dimensional layer of Co-MOF, XPS of CoFe-LDH/Co-MOF, full CV curves of the Co-MOF array, optimized structure of Co-MOF, and charge density distribution of Co-MOF after structure optimization (PDF)

Accession Codes

CCDC 2301027 contains the supplementary crystallographic data for this paper. These data can be obtained free of charge via www.ccdc.cam.ac.uk/data_request/cif, or by emailing data_request@ccdc.cam.ac.uk, or by contacting The Cambridge Crystallographic Data Centre, 12 Union Road, Cambridge CB2 1EZ, UK; fax: +44 1223 336033.

■ AUTHOR INFORMATION

Corresponding Author

Ani Wang − *College of Chemistry and Chemical Engineering, Qingdao University, Qingdao, Shandong 266071, P. R. China;* orcid.org/0000-0002-5669-1424; Email: wangani@qdu.edu.cn

Authors

Guoying Yang − *College of Chemistry and Chemical Engineering, Qingdao University, Qingdao, Shandong 266071, P. R. China*

Yijin Song − *College of Chemistry and Chemical Engineering, Qingdao University, Qingdao, Shandong 266071, P. R. China*

Songde Han − *College of Chemistry and Chemical Engineering, Qingdao University, Qingdao, Shandong 266071, P. R. China;* orcid.org/0000-0001-6335-8083

Zhen-Zhen Xue − *College of Chemistry and Chemical Engineering, Qingdao University, Qingdao, Shandong 266071, P. R. China;* orcid.org/0000-0001-8183-088X

De-Xuan Liu − *College of Chemistry and Chemical Engineering, Qingdao University, Qingdao, Shandong 266071, P. R. China*

Guoming Wang − *College of Chemistry and Chemical Engineering, Qingdao University, Qingdao, Shandong 266071, P. R. China;* orcid.org/0000-0003-0156-904X

Complete contact information is available at: https://pubs.acs.org/10.1021/acs.inorgchem.4c00021

Notes

The authors declare no competing financial interest.

■ ACKNOWLEDGMENTS

We acknowledge the financial support from the National Natural Science Foundation of China (grant no. 22201153) and Natural Science Foundation of Shandong Province (ZR2020QB140).

■ REFERENCES

(1) Zeng, S.-P.; Shi, H.; Dai, T.-Y.; Liu, Y.; Wen, Z.; Han, G.-F.; Wang, T.-H.; Zhang, W.; Lang, X.-Y.; Zheng, W.-T.; Jiang, Q. Lamella-heterostructured nanoporous bimetallic iron-cobalt alloy/oxyhydroxide and cerium oxynitride electrodes as stable catalysts for oxygen evolution. *Nat. Commun.* **2023**, *14*, 1811.

(2) Cao, C.; Ma, D. D.; Xu, Q.; Wu, X. T.; Zhu, Q. L. Semisacrificial Template Growth of Self-Supporting MOF Nanocomposite Electrode for Efficient Electrocatalytic Water Oxidation. *Adv. Funct. Mater.* **2018**, *29*, 1807418.

(3) Zhao, S.; Tan, C.; He, C.-T.; An, P.; Xie, F.; Jiang, S.; Zhu, Y.; Wu, K.-H.; Zhang, B.; Li, H.; Zhang, J.; Chen, Y.; Liu, S.; Dong, J.; Tang, Z. Structural transformation of highly active metal−organic framework electrocatalysts during the oxygen evolution reaction. *Nature Energy* **2020**, *5*, 881−890.

(4) Miao, K.; Jiang, W.; Chen, Z.; Luo, Y.; Xiang, D.; Wang, C.; Kang, X. Hollow-Structured and Polyhedron-Shaped High Entropy Oxide toward Highly Active and Robust Oxygen Evolution Reaction in a Full pH Range. *Adv. Mater.* **2024**, *36*, 2307294.

(5) Xue, Y.; Ma, G.; Wang, X.; Jin, M.; Akinoglu, E. M.; Luo, D.; Shui, L. Bimetallic Hollow Tubular $NiCoO_x$ as a Bifunctional Electrocatalyst for Enhanced Oxygen Reduction and Evolution Reaction. *ACS Appl. Mater. Interfaces* **2021**, *13*, 7334−7342.

(6) He, P.; Yu, X.-Y.; Lou, X. W. Carbon-Incorporated Nickel-Cobalt Mixed Metal Phosphide Nanoboxes with Enhanced Electrocatalytic Activity for Oxygen Evolution. *Angew. Chem., Int. Ed.* **2017**, *56*, 3897−3900.

(7) Niu, Q.; Yang, M.; Luan, D.; Li, N. W.; Yu, L.; Lou, X. W. Construction of Ni-Co-Fe Hydr(oxy)oxide@Ni-Co Layered Double Hydroxide Yolk-Shelled Microrods for Enhanced Oxygen Evolution. *Angew. Chem., Int. Ed.* **2022**, *61*, No. e202213049.

(8) Pei, Z.; Lu, X. F.; Zhang, H.; Li, Y.; Luan, D.; Lou, X.-W. Highly Efficient Electrocatalytic Oxygen Evolution Over Atomically Dispersed Synergistic Ni/Co Dual Sites. *Angew. Chem., Int. Ed.* **2022**, *61*, No. e202207537.
(9) Wang, S.; Ning, X.; Cao, Y.; Chen, R.; Lu, Z.; Hu, J.; Xie, J.; Hao, A. Construction of an Advanced NiFe-LDH/MoS2−Ni3S2/NF Heterostructure Catalyst toward Efficient Electrocatalytic Overall Water Splitting. *Inorg. Chem.* **2023**, *62*, 6428−6438.
(10) Guo, M.-L.; Wu, Z.-Y.; Zhang, M.-M.; Huang, Z.-J.; Zhang, K.-X.; Wang, B.-R.; Tu, J.-C. Coupling interface constructions of $FeOOH/NiCo_2S_4$ by microwave-assisted method for efficient oxygen evolution reaction. *Rare Metals* **2023**, *42*, 1847−1857.
(11) Fei, L.; Sun, H.; Xu, X.; Li, Y.; Ran, R.; Zhou, W.; Shao, Z. Understanding the bifunctional catalytic ability of electrocatalysts for oxygen evolution reaction and urea oxidation Reaction: Recent advances and perspectives. *Chemical Engineering Journal* **2023**, *471*, No. 144660.
(12) Liu, X. T.; Qian, B. B.; Zhang, D. S.; Yu, M. H.; Chang, Z.; Bu, X. H. Recent progress in host−guest metal−organic frameworks: Construction and emergent properties. *Chem. Soc. Rev.* **2023**, *476*, No. 214921.
(13) Zhang, B.; Xu, J.; Li, C. T.; Huang, H. L.; Chen, M. X.; Yu, M. H.; Chang, Z.; Bu, X. H. Facile Tuned TSCT-TADF in Donor-Acceptor MOF for Highly Adjustable Photonic Modules based on Heterostructures Crystals. *Angew. Chem., Int. Ed.* **2023**, *62*, No. e202303262.
(14) Liu, X.-T.; Hua, W.; Nie, H.-X.; Chen, M.; Chang, Z.; Bu, X.-H. Manipulating spatial alignment of donor and acceptor in host−guest MOF for TADF. *National Science Review* **2022**, *9*, nwab222.
(15) Yu, M.-H.; Geng, L.; Chang, Z.; Bu, X.-H. Coordination Bonding Directed Molecular Assembly toward Functional Metal−Organic Frameworks: From Structural Regulation to Properties Modulation. *Accounts of Materials Research* **2023**, *4*, 839−853.
(16) Wang, H.-F.; Chen, L.; Pang, H.; Kaskel, S.; Xu, Q. MOF-derived electrocatalysts for oxygen reduction, oxygen evolution and hydrogen evolution reactions. *Chem. Soc. Rev.* **2020**, *49*, 1414−1448.
(17) Qian, Y.; Zhang, F.; Zhao, S.; Bian, C.; Mao, H.; Kang, D. J.; Pang, H. Recent progress of metal-organic framework-derived composites: Synthesis and their energy conversion applications. *Nano Energy* **2023**, *111*, No. 108415.
(18) Huang, M.; Cao, C.; Liu, L.; Wei, W.; Zhu, Q.-L.; Huang, Z. Controlled synthesis of MOF-derived hollow and yolk−shell nanocages for improved water oxidation and selective ethylene glycol reformation. *eScience* **2023**, *3*, No. 100118, DOI: 10.1016/j.esci.2023.100118.
(19) Jiao, L.; Wei, W.; Li, X.; Hong, C.-B.; Han, S.-G.; Khan, M. I.; Zhu, Q.-L. Value-added formate production from selective ethylene glycol oxidation based on cost-effective self-supported MOF nanosheet arrays. *Rare Metals* **2022**, *41*, 3654−3661.
(20) Shi, F.; Wang, Z.; Zhu, K.; Zhu, X.; Yang, W. Enhancing activity and stability of Co-MOF-74 for oxygen evolution reaction by wrapping polydopamine. *Electrochim. Acta* **2022**, *416*, No. 140293.
(21) Ge, K.; Sun, S.; Zhao, Y.; Yang, K.; Wang, S.; Zhang, Z.; Cao, J.; Yang, Y.; Zhang, Y.; Pan, M.; Zhu, L. Facile Synthesis of Two-Dimensional Iron/Cobalt Metal-Organic Framework for Efficient Oxygen Evolution Electrocatalysis. *Chemie-International Edition* **2021**, *60*, 12097−12102.
(22) Liao, Y.; Xiao, Y.; Li, Z.; Zhou, X.; Liu, J.; Guo, F.; Li, J.; Li, Y. Structural Engineering of Co-Metal-Organic Frameworks via Ce Incorporation for Improved Oxygen Evolution. *Small* **2023**, 2307685.
(23) Yao, Y.; Yang, C.; Sun, S.; Zhang, H.; Geng, M.; He, X.; Dong, K.; Luo, Y.; Zheng, D.; Zhuang, W.; Alfaifi, S.; Farouk, A.; Hamdy, M. S.; Tang, B.; Zhu, S.; Sun, X.; Hu, W. Boosting Alkaline Seawater Oxidation of CoFe-layered Double Hydroxide Nanosheet Array by Cr Doping. *Small* **2023**, 2307294.
(24) Yao, H.; Wang, S.; Cao, Y.; Chen, R.; Lu, Z.; Hu, J.; Xie, J.; Hao, A. High-performance bifunctional electrocatalysts of CoFe-LDH/$NiCo_2O_4$ heterostructure supported on nickel foam for effective overall water splitting. *J. Alloys Compd.* **2022**, *926*, No. 166846.
(25) Tang, R.; Ying, M.; Zhang, X.; Zheng, R.; Huang, J. Interfacial Heterojunction-Engineered Fe_2O_3/CoFe-Layered Double Hydroxide Catalyst for the Electrocatalytic Oxygen Evolution Reaction. *Energy Fuels* **2022**, *36*, 11584−11590.
(26) Hu, L.; Tian, L.; Ding, X.; Wang, X.; Wang, X.; Qin, Y.; Gu, W.; Shi, L.; Zhu, C. p-d hybridization in CoFe LDH nanoflowers for efficient oxygen evolution electrocatalysis. *Inorganic Chemistry Frontiers* **2022**, *9*, 5296−5304.
(27) Xiao, M.; Wu, C.; Zhu, J.; Zhang, C.; Li, Y.; Lyu, J.; Zeng, W.; Li, H.; Chen, L.; Mu, S. In situ generated layered NiFe-LDH/MOF heterostructure nanosheet arrays with abundant defects for efficient alkaline and seawater oxidation. *Nano Research* **2023**, *16*, 8945−8952.
(28) Zhang, Z.; Ma, X.; Han, X.; Cui, H.; Lu, Y.; Liu, S.; Liu, Y. Straightforward construction of hollow polyoxometalate-based metal-organic framework via pseudo-homoepitaxial growth. *Science China Chemistry* **2022**, *65*, 1921−1928.
(29) Wang, W.; Yan, H.; Anand, U.; Mirsaidov, U. Visualizing the Conversion of Metal−Organic Framework Nanoparticles into Hollow Layered Double Hydroxide Nanocages. *J. Am. Chem. Soc.* **2021**, *143*, 1854−1862.
(30) Wang, L.; Wang, A.; Fan, W.; Pan, J.; Xue, Z.; Wang, G. Ligand-Assisted Controllable Growth of Self-Supporting Ultrathin Two-Dimensional Metal-Organic Framework Nanosheet Electrodes for an Efficient Oxygen Evolution Reaction. *Inorg. Chem.* **2022**, *61*, 14899−14907.
(31) Chen, D.; Ji, X.; Zhou, X.; Sun, Q.; Xu, S.; Mao, L.; Guo, Z.; Guan, J.; Li, T.-T.; Qian, J. MOF-on-MOF-derived hollow $FeNi_3$/N-doped carbon nanorods for efficient oxygen evolution. *Chemical Engineering Journal* **2023**, *470*, No. 144418.
(32) Li, Z.; Song, M.; Zhu, W.; Zhuang, W.; Du, X.; Tian, L. MOF-derived hollow heterostructures for advanced electrocatalysis. *Coord. Chem. Rev.* **2021**, *439*, No. 213946.
(33) Xu, M.; Li, X.; Sha, J.-Q.; Tong, Z.; Li, Q.; Liu, C. Hollow POM@MOF-derived Porous $NiMo_6Co_3O_4$ for Biothiol Colorimetric Detection. *Chem.—Eur. J.* **2021**, *27*, 9141−9151.
(34) Zhang, W.; Jiang, X.; Zhao, Y.; Carne-Sanchez, A.; Malgras, V.; Kim, J.; Kim, J. H.; Wang, S.; Liu, J.; Jiang, J.-S.; Yamauchi, Y.; Hu, M. Hollow carbon nanobubbles: monocrystalline MOF nanobubbles and their pyrolysis. *Chemical Science* **2017**, *8*, 3538−3546.
(35) Fan, W.; Wang, A.; Wang, L.; Li, X.-Y.; Wang, W.; Pan, J.; Xue, Z.-Z. Self-Dissociation-Oriented Growth of Ultrathin Metal-Organic Framework Nanosheet Arrays for Efficient Oxygen Evolution. *Cryst. Growth Des.* **2023**, *23*, 3297−3307.
(36) Wang, L.; Wang, A.; Xue, Z.-Z.; Hu, J.-X.; Wang, G.-M.; Han, S.-D. Ultrathin Two-Dimensional Polyoxometalate-Based Metal-Organic Framework Nanosheets for Efficient Electrocatalytic Hydrogen Evolution. *Inorg. Chem.* **2022**, *61*, 18311−18317.
(37) Wang, L.; Wang, A. N.; Xue, Z. Z.; Wang, Y.-R.; Han, S. D.; Wang, G. M. *In situ* growth of polyoxometalate-based metal-organic framework nanoflower arrays for efficient hydrogen evolution. *Chin. Chem. Lett.* **2023**, *34*, 107414.
(38) Wang, Y.; Wang, A.; Xue, Z.; Wang, L.; Li, X.; Wang, G. Ultrathin metal-organic framework nanosheet arrays and derived self-supported electrodes for overall water splitting. *Journal of Materials Chemistry A* **2021**, *9*, 22597−22602.
(39) Chen, C.; Tuo, Y.; Lu, Q.; Lu, H.; Zhang, S.; Zhou, Y.; Zhang, J.; Liu, Z.; Kang, Z.; Feng, X.; Chen, D. Hierarchical trimetallic Co-Ni-Fe oxides derived from core-shell structured metal-organic frameworks for highly efficient oxygen evolution reaction. *Appl. Catal., B* **2021**, *287*, No. 119953.
(40) Cheng, Y.; Yin, Z.; Ma, W.-M.; He, Z.-X.; Yao, X.; Lv, W.-Y. Alkali-Induced In Situ Formation of Amorphous $Ni_xFe_{1-x}OH_2$ from a Linear $M_3(COO)_6$ Based MOF Template for Overall Electrochemical Water Splitting. *Inorg. Chem.* **2022**, *61*, 3327−3336.
(41) Sankar, S. S.; Keerthana, G.; Manjula, K.; Sharad, J. H.; Kundu, S. Electrospun Fe-Incorporated ZIF-67 Nanofibers for Effective Electrocatalytic Water Splitting. *Inorg. Chem.* **2021**, *60*, 4034−4046.
(42) Abdelkader-Fernandez, V. K.; Fernandes, D. M.; Balula, S. S.; Cunha-Silva, L.; Jose Perez-Mendoza, M.; Lopez-Garzon, F. J.;

https://doi.org/10.1021/acs.inorgchem.4c00021
Inorg. Chem. 2024, 63, 5634−5641

Fernando Pereira, M.; Freire, C. Noble-Metal-Free MOF-74-Derived Nanocarbons: Insights on Metal Composition and Doping Effects on the Electrocatalytic Activity Toward Oxygen Reactions. *ACS Applied Energy Materials* **2019**, *2*, 1854−1867.
(43) Zha, Q.; Yuan, F.; Qin, G.; Ni, Y. Cobalt-Based MOF-on-MOF Two-Dimensional Heterojunction Nanostructures for Enhanced Oxygen Evolution Reaction Electrocatalytic Activity. *Inorg. Chem.* **2020**, *59*, 1295−1305.
(44) Fu, R.; Jiao, Q.; Feng, X.; Zhu, H.; Yang, C.; Feng, C.; Li, H.; Zhang, Y.; Shi, D.; Wu, Q.; Zhao, Y. Metal-organic frameworks derived Ni_5P_4/NC@CoFeP/NC composites for highly efficient oxygen evolution reaction. *J. Colloid Interface Sci.* **2022**, *617*, 585−593.
(45) Gupta, A.; Allison, C. A.; Ellis, M. E.; Choi, J.; Davis, A.; Srivastava, R.; de Souza, F. M.; Neupane, D.; Mishra, S. R.; Perez, F.; Kumar, A.; Gupta, R. K.; Dawsey, T. Cobalt metal -organic framework derived cobalt-nitrogen-carbon material for overall water splitting and supercapacitor. *Int. J. Hydrogen Energy* **2023**, *48*, 9551−9564.
(46) Peera, S. G.; Balamurugan, J.; Kim, N. H.; Lee, J. H. Sustainable Synthesis of Co@NC Core Shell Nanostructures from Metal Organic Frameworks via Mechanochemical Coordination Self-Assembly: An Efficient Electrocatalyst for Oxygen Reduction Reaction. *Small* **2018**, *14*, 1800441.
(47) Wang, H.; Yin, F.; Li, G.; Chen, B.; Wang, Z. Preparation, characterization and bifunctional catalytic properties of MOF(Fe/Co) catalyst for oxygen reduction/evolution reactions in alkaline electrolyte. *Int. J. Hydrogen Energy* **2014**, *39*, 16179−16186.
(48) Cheng, C.-C.; Lin, T.-Y.; Ting, Y.-C.; Lin, S.-H.; Choi, Y.; Lu, S.-Y. Metal-organic frameworks stabilized Mo and W binary single-atom catalysts as high performance bifunctional electrocatalysts for water electrolysis. *Nano Energy* **2023**, *112*, No. 108450.
(49) Li, X.; Wu, X.; Li, B.; Zhang, S.; Liu, Y.; Li, Z.; Zhang, D.; Wang, X.; Sun, Q.; Gao, D.; Zhang, C.; Huang, W.-H.; Chueh, C.-C.; Chen, C.-L.; Yang, S.; Xiao, S.; Wang, Z.; Zhu, Z. Efficient Solar-Driven Water Splitting Enabled by Perovskite Photovoltaics and a Halogen-Modulated Metal-Organic Framework Electrocatalyst. *ACS Nano* **2023**, *17*, 23478−23487.
(50) Ashoori, A.; Noori, A.; Rahmanifar, M. S.; Morsali, A.; Hassani, N.; Neek-Amal, M.; Ghasempour, H.; Xia, X.; Zhang, Y.; El-Kady, M. F.; Kaner, R. B.; Mousavi, M. F. Tailoring Metal-Organic Frameworks and Derived Materials for High-Performance Zinc-Air and Alkaline Batteries. *ACS Appl. Mater. Interfaces* **2023**, *15*, 30220−30239.
(51) Mu, G.; Wang, G.; Huang, Q.; Miao, Y.; Wen, D.; Lin, D.; Xu, C.; Wan, Y.; Xie, F.; Guo, W.; Zou, R. A Kinetic Control Strategy for One-Pot Synthesis of Efficient Bimetallic Metal-Organic Framework/Layered Double Hydroxide Heterojunction Oxygen Evolution Electrocatalysts. *Adv. Funct. Mater.* **2023**, *33*, 2211260.
(52) Wang, X.-Y.; Zhu, M.; Bian, Q.-N.; Guo, B.-S.; Kong, W.-Q.; Wang, C.-B.; Feng, Y.-Y. Fe-Based Metal-Organic Framework-Ni_3S_2 Heterostructure Nanocomposites for Efficient Oxygen Evolution Reaction at High Current Densities. *ACS Applied Nano Materials* **2023**, *6*, 5200−5210.
(53) Long, X.; Li, J.; Xiao, S.; Yan, K.; Wang, Z.; Chen, H.; Yang, S. A Strongly Coupled Graphene and FeNi Double Hydroxide Hybrid as an Excellent Electrocatalyst for the Oxygen Evolution Reaction. *Angew. Chem., Int. Ed.* **2014**, *53*, 7584−7588.
(54) Xie, L.; Li, X.; Wang, B.; Meng, J.; Lei, H.; Zhang, W.; Cao, R. Molecular Engineering of a 3D Self-Supported Electrode for Oxygen Electrocatalysis in Neutral Media. *Angew. Chem., Int. Ed.* **2019**, *58*, 18883−18887.
(55) Chen, X.; Wang, Q.; Cheng, Y.; Xing, H.; Li, J.; Zhu, X.; Ma, L.; Li, Y.; Liu, D. S-Doping Triggers Redox Reactivities of Both Iron and Lattice Oxygen in FeOOH for Low-Cost and High-Performance Water Oxidation. *Adv. Funct. Mater.* **2022**, *32*, 2112674.
(56) Huang, W.; Li, J.; Liao, X.; Lu, R.; Ling, C.; Liu, X.; Meng, J.; Qu, L.; Lin, M.; Hong, X.; Zhou, X.; Liu, S.; Zhao, Y.; Zhou, L.; Mai, L. Ligand Modulation of Active Sites to Promote Electrocatalytic Oxygen Evolution. *Adv. Mater.* **2022**, *34*, 2200270.
(57) Mhadeshwar, A. B.; Vlachos, D. G. Hierarchical, multiscale surface reaction mechanism development: CO and H_2 oxidation, water-gas shift, and preferential oxidation of CO on Rh. *J. Catal.* **2005**, *234*, 48−63.
(58) Fei, H.; Dong, J.; Feng, Y.; Allen, C. S.; Wan, C.; Volosskiy, B.; Li, M.; Zhao, Z.; Wang, Y.; Sun, H.; An, P.; Chen, W.; Guo, Z.; Lee, C.; Chen, D.; Shakir, I.; Liu, M.; Hu, T.; Li, Y.; Kirkland, A. I.; Duan, X.; Huang, Y. General synthesis and definitive structural identification of MN_4C_4 single-atom catalysts with tunable electrocatalytic activities. *Nat. Catal.* **2018**, *1*, 63−72.
(59) Huang, H.; Zhou, S.; Yu, C.; Huang, H.; Zhao, J.; Dai, L.; Qiu, J. Rapid and energy-efficient microwave pyrolysis for high-yield production of highly-active bifunctional electrocatalysts for water splitting. *Energy Environ. Sci.* **2020**, *13*, 545−553.
(60) Xiao, Z.; Wang, Y.; Huang, Y.-C.; Wei, Z.; Dong, C.-L.; Ma, J.; Shen, S.; Li, Y.; Wang, S. Filling the oxygen vacancies in Co_3O_4 with phosphorus: an ultra-efficient electrocatalyst for overall water splitting. *Energy Environ. Sci.* **2017**, *10*, 2563−2569.
(61) Zhang, J.; Hao, L.; Chen, Z.; Gao, Y.; Wang, H.; Zhang, Y. Facile synthesis of Co−Fe layered double hydroxide nanosheets wrapped on Ni-doped nanoporous carbon nanorods for oxygen evolution reaction. *J. Colloid Interface Sci.* **2023**, *650*, 816−824.
(62) Li, W.; Li, C.; Dong, H.; Zhang, X.; Liu, J.; Song, M.; Wang, G.; Zhao, L.; Sheng, H.; Chen, B.; Zhang, H. Expediting Oxygen Evolution by Optimizing Cation and Anion Complexity in Electrocatalysts Based on Metal Phosphorous Trichalcogenides. *Angew. Chem., Int. Ed.* **2023**, *62*, No. e2022145.
(63) Lee, J.; Kumar, A.; Yang, T.; Liu, X.; Jadhav, A. R.; Park, G. H.; Hwang, Y.; Yu, J.; Nguyen, C. T. K.; Liu, Y.; Ajmal, S.; Kim, M. G.; Lee, H. Stabilizing the OOH* intermediate via pre-adsorbed surface oxygen of a single Ru atom-bimetallic alloy for ultralow overpotential oxygen generation. *Energy Environ. Sci.* **2020**, *13*, 5152−5164.
(64) Camacho-Forero, L. E.; Godinez-Salomon, F.; Ramos-Sanchez, G.; Rhodes, C. P.; Balbuena, P. B. Theoretical and experimental study of the effects of cobalt and nickel doping within IrO_2 on the acidic oxygen evolution reaction. *J. Catal.* **2022**, *408*, 64−80.
(65) Cai, G.; Zhang, W.; Jiao, L.; Yu, S.-H.; Jiang, H.-L. Template-Directed Growth of Well-Aligned MOF Arrays and Derived Self-Supporting Electrodes for Water Splitting. *Chem.* **2017**, *2*, 791−802.

https://doi.org/10.1021/acs.inorgchem.4c00021
Inorg. Chem. 2024, 63, 5634−5641